Estimation of diurnal emissions of CO$_2$ from thermal power plants using spaceborne IPDA lidar

Xuanye Zhang[1], Hailong Yang[2], Lingbing Bu[1], Zengchang Fan[1], Wei Xiao[3], Binglong Chen[4], Lu Zhang[4], Sihan Liu[5], Zhongting Wang[5], Jiqiao Liu[6], Weibiao Chen[6] and Xuhui Lee[7]

[1]School of Atmosphere Physics, Nanjing University of Information Science & Technology, Nanjing, 210044, China
[2]Shanghai Satellite Engineering Research Institute, Shanghai, 201109, China
[3]Nanjing University of Information Science and Technology, Yale-NUIST Center on Atmospheric Environment, Nanjing, 210044, China
[4]Key Laboratory of Radiometric Calibration and Validation for Environmental Satellites, National Satellite Meteorological Center (National Center for Space Weather), China Meteorological Administration. Innovation Center for FengYun Meteorological Satellite (FYSIC), Beijing, 100081, China
[5]Satellite Application Center for Ecology and Environment, Ministry of Ecology and Environment, Beijing, China
[6]Key Laboratory of Space Laser Communication and Detection Technology, Shanghai Institute of Optics and Fine Mechanics, Chinese Academy Of Sciences, Shanghai, China
[7]Yale University, School of the Environment, NewHaven, CT, America

Correspondence to: Lingbing Bu (lingbingbu@nuist.edu.cn)

Abstract. Coal-fired power plants are a major source of global carbon emissions, and accurately accounting for these significant emission sources is crucial in addressing global warming. Many previous studies have used Gaussian plume models to estimate power plant emissions, but there is a gap in observation capabilities for high-latitude regions and nighttime emissions. However, large emitting power plants exist in high-latitude areas. The DQ-1 satellite is equipped with the world's first active remote sensing lidar for detecting CO$_2$ column concentrations, which, compared to passive remote sensing satellites, enables observations in these regions. This paper applies a two-dimensional Gaussian plume model to the XCO$_2$ results from the DQ-1 satellite and analyses the instantaneous CO$_2$ emissions of 10 power plants globally. Among these, 15 cases of data are from nighttime observations, and 3 cases are from power plants located above 60° N latitude. The estimation results show good consistency when compared with emission inventories such as Climate TRACE and Carbon Brief, with a correlation coefficient R = 0.97. The correlation coefficient between the model fits and satellite observations ranges from 0.49 to 0.88, and the overall relative random error in the estimates is 15.11 %. This paper also analyses the diurnal ~~and seasonal variations~~differences in CO$_2$ emissions from ~~the~~ power plants~~, finding that emission variations align~~ and finds emissions fluctuations directly correlated with ~~changes in~~regional electricity ~~consumption in the surrounding regions.~~demand dynamics. This method is very effective for monitoring ~~the diurnal variations of~~emissions from strong ~~emission~~point sources ~~like~~such as power plants.

1 Introduction

Global warming is caused by the continuous increase of greenhouse gases in the atmosphere. The Kyoto Protocol under the United Nations Framework Convention on Climate Change classifies six gases, including carbon dioxide (CO$_2$), methane

35 (CH$_4$), nitrous oxide (N$_2$O), hydrofluorocarbons (HFCS), perfluorocarbons (PFCS), and sulfur hexafluoride (SF$_6$), as major greenhouse gases, with CO$_2$ being the largest contributor and a key anthropogenic greenhouse gas (Protocol, 1997). Changes in atmospheric composition due to industrial development, land-use changes, deforestation, and livestock farming have led to global warming and a series of severe events impacting the Earth's ecological environment, such as frequent natural disasters. These effects are further exacerbated by increasing greenhouse gas emissions (Arias et al., 2021; Searchinger et al., 2018).

40 Currently, greenhouse gas emissions are accelerating, with global annual CO$_2$ emissions rising from 27 Pg to 49 Pg over the past 40 years (Friedlingstein et al., 2022). In response to the severe challenges posed by climate change, countries worldwide are actively participating in CO$_2$ growth control initiatives and formulating strategies. China aims to peak CO$_2$ emissions by 2030 and achieve carbon neutrality by 2060 to curb the sharp rise in atmospheric CO$_2$ concentrations (Li et al., 2022).

Effective control of CO$_2$ emissions relies on accurate, timely, and transparent monitoring. Currently, countries assess emission

45 reduction measures through greenhouse gas inventories, but challenges such as data lag, inconsistent standards, and insufficient information transparency undermine comparability and credibility (Tubiello et al., 2015; Peters et al., 2012). For monitoring urban CO$_2$ emissions, most methods employ emission models based on inventory data, following a "bottom-up" approach (Gurney et al., 2017; Turnbull et al., 2018; Lauvaux et al., 2016). ~~The~~In recent years, some studies have used "top-down" approaches, such as combining satellite observation data with WRF-STILT ~~model is one of the most widely used atmospheric~~

50 ~~transport~~or WRF-Chem models ~~for simulating~~to quantify urban greenhouse gas ~~concentrations, but its performance in nighttime CO$_2$ simulation is hindered by the lack of emission height information in inventories~~emissions (Turner et al., 2020; Pillai et al., 2012; Hu et al., 2022; Wu et al., 2018; Ye et al., 2020). For small point sources like power plants, airborne or ground-based monitoring is typically used to measure CO$_2$ concentrations. Relevant studies have employed the mass balance method to assess CO$_2$ emissions from power plants and cities through airborne observations (Ahn et al., 2020). Some research

55 teams have also utilized the inverse Gaussian plume model with MAMAP instruments to remotely sense the column-averaged dry-air mole fractions of CO$_2$ (XCO$_2$) from power plants (Krings et al., 2018; Krings et al., 2011). Ground-based equipment, such as portable Fourier transform spectrometers (EM27/SUN), combined with the Gaussian plume model and the cross-sectional flux method, has also been used to measure ground-level CO$_2$ concentrations for specific power plants and urban areas (Ohyama et al., 2021; Luther et al., 2019).

60 Satellite remote sensing technology holds significant potential for monitoring atmospheric CO$_2$ due to its capability for long-term, periodic observations on a global scale (Zhang et al., 2021). Monitoring point source emissions using satellites is challenging. ~~Although~~Compared to the ~~accuracy of~~budgeting approach for estimating point source emissions (Amediek et al., 2017), the Gaussian plume model (GPM) is highly influenced by the precision of atmospheric background driving fields (Nassar et al., 2017; Brunner et al., 2023), it is not constrained by the spatial resolution of the model, and ~~remains~~is more stable

65 and effective in ~~simulating~~modelling point source dispersion if limited by the background wind field (Toja-Silva et al., 2017; Schwandner et al., 2017). The Orbiting Carbon Observatory-2 (OCO-2) ~~is widely used due to its~~has high measurement accuracy and stable results (Sheng et al., 2023; Crisp et al., 2017; Miller et al., 2007), and its XCO$_2$ product can be used in conjunction with GPM for the estimation of point source emissions. When it passes downwind of a single point source, a

2

significant increase in XCO_2 can be observed due to strong CO_2 emissions, and by fitting the observed XCO_2 with plume simulations, instantaneous CO_2 emissions can be quantified (Nassar et al., 2017). In recent years, a series of studies have been conducted to estimate CO_2 emissions from power plants, volcanoes, and cities based on OCO-2's XCO_2 data (Nassar et al., 2017; Guo et al., 2023; Zheng et al., 2020; Crisp et al., 2017). Nassar et al. used the Gaussian plume model to estimate CO_2 emissions and uncertainties from 20 power plants and related facilities in the U.S., India, South Africa, Poland, Russia, and South Korea, noting an average difference of 15.1 % between the estimated emissions and reported values for U.S. power plants (Nassar et al., 2021). However, OCO-2/OCO-3~~/GOSAT~~ are passive remote sensing satellites, which present data gaps in high-latitude and nighttime observations, and their spatial resolution of ~~approximately 3~~1.5 km × 2.25 km poses limitations for monitoring small-scale strong point sources (Shi et al., 2023~~; Taylor et al., 2022~~; Eldering et al., 2019). For power plants, due to variations in power demand, nighttime emissions differ significantly from daytime levels, and there may be instances of illegal nighttime over-emissions at certain plants, making nighttime CO_2 emission observations necessary (Letu et al., 2014).

Spaceborne active remote sensing of CO_2 primarily employs the integrated path differential absorption (IPDA) principle (Ehret et al., 2008), enabling nighttime and high-latitude observations. Kiemle et al. discussed the ability to monitor CO_2 emissions using spaceborne lidar in combination with the plume model and a mass budget approach (Kiemle et al., 2017). Recent studies have demonstrated the feasibility of laser-based detection techniques for CO_2 emission monitoring (Menzies et al., 2022; Wolff et al., 2024). In 2022, China launched the Atmospheric Environment Monitoring Satellite (AEMS, also known as DQ-1), the first equipped with spaceborne IPDA ~~(Integrated Path Differential Absorption)~~ lidar, capable of global XCO_2 measurements. This technology addresses the gap in XCO_2 observations at high latitudes and during nighttime (Cai et al., 2022; Fan et al., 2024). ~~Additionally, the XCO₂ measurement accuracy is~~ The XCO_2 results from DQ-1 were validated against TCCON observations, showing an average deviation of less than 1 ppm~~, with a~~ at a 50 km (149 footprints averaged) resolution (Zhang et al., 2024). Additionally, its satellite footprint interval ~~of~~is 330 meters, significantly enhancing ~~spatial and temporal coverage~~ the estimation accuracy for small power ~~plant monitoring (Zhang et al., 2024;~~ plants. (Zhang et al., 2023). Han et al. applied the EMI-GATE model, based on the Gaussian plume, to evaluate power plant emissions using DQ-1 data (Han et al., 2024). ~~Compared to Han et al.'s research, this study employs a different approach to the Gaussian plume model, resulting in lower random errors in emission estimates.~~The main differences between the Gaussian plume model used in this study and the EMI-GATE model used by Han et al. are the methods used to calculate the Gaussian plume model parameters such as the atmospheric instability parameters and the wind field, as well as the fact that we additionally quantify the uncertainty due to atmospheric instability. This paper also analyses two years of satellite data, examining emission variations of a single power plant over time. Section 2 introduces the data sources and methods of this study. In Section 3, the improved Gaussian plume model is integrated with DQ-1 satellite observations, selecting 10 globally high-emission power plants, including 15 nighttime observations and 23 observations of power plants in high-latitude regions, estimating their CO_2 emissions. Analyses of diurnal and seasonal variations in CO_2 emissions are also conducted. Section 4 provides a summary and discusses the potential applications of the Gaussian plume model with spaceborne IPDA lidar.

2 Data and Methodology

2.1 Data

2.1.1 DQ-1 satellite data

105 On 16 April 2022, China launched the world's first satellite designed for active remote sensing of carbon dioxide. This satellite is equipped with an Aerosol and Carbon Dioxide Laser Detection Lidar (ACDL). The primary scientific objectives are to measure high-resolution vertical profiles and the optical properties of global atmospheric aerosols and clouds, as well as to obtain global atmospheric CO_2 column concentration data. This provides precise quantitative information for studies on CO_2 sources and sinks (Fan et al., 2024). The satellite utilizes Integrated Path Differential Absorption (IPDA) technology to measure

110 CO_2 column concentration. It employs a 1572 nm pulsed laser and the IPDA lidar method, using two wavelengths (λon and λoff, corresponding to regions of strong and weak absorption lines). The difference in absorption cross-sections (σ) between these two wavelengths is used to determine the CO_2 column concentration. ~~On orbit tests of the lidar~~XCO$_2$ can be calculated using these two wavelength echo signal strengths combined with following equation (Ehret et al., 2008):

$$XCO_2 = \frac{DAOD}{IWF} = \frac{\frac{1}{2} ln \frac{P_{off}E_{on}}{P_{on}E_{off}}}{\int_{P_{TOA}}^{P_G} \frac{\Delta\sigma(p,T)}{(m_{dryair} + \rho_{H_2O}(p)m_{H_2O})g} dp} \tag{1}$$

115 $DAOD$ is Differential Absorption Optical Depth, IWF is the integral weight function, P_{on}/P_{off}, represents the echo power of the two laser beams, E_{on}/E_{off} represents the emitted power, p_{TOA} and p_G are the pressure at the top of the atmosphere and at the ground, $\Delta\sigma(p,T)$ represents differential absorption cross-section, m_{dryair} is the molecular mass of dry air, ρ_{H_2O} is the relative humidity of the air. On-orbit tests of ACDL have yielded high-precision remote sensing data, confirming that the CO_2 column concentration measurement accuracy is better than 1 ppm. Notably, this satellite provides the first global CO_2 column

120 concentration measurements at night and over the poles (Zhang et al., 2024). The satellite's footprint spacing of 330 meters ensures high spatial resolution. This study utilizes the satellite's L2D product, which includes global XCO_2 data derived from raw observation data combined with the IPDA lidar inversion method. The datasets include XCO_2 values, uncertainty for XCO_2, and the corresponding surface elevation and geographic coordinates for each footprint.

2.1.2 Wind data

125 This study utilizes horizontal (U) and vertical (V) wind components from the fifth-generation European Centre for Medium-Range Weather Forecasts (ECMWF) global climate atmospheric reanalysis dataset (ERA-5). The dataset features a temporal resolution of 1 hour, a spatial resolution of 0.25°, and includes 37 vertical pressure levels (Hersbach et al., 2020). A four-dimensional interpolation method is applied to the U and V vectors at the plume lift height, which is set to a default chimney height of 240 meters and a plume vertical lift height of 250 meters (Hu and Shi, 2021). To evaluate the impact of wind speed

130 uncertainty on power plant emission predictions, the study also compares results using MERRA-2 horizontal wind data (Gelaro

et al., 2017). ~~Ground-level~~In this study, atmospheric instability is calculated from surface 2 m wind ~~speed~~ speeds and cloud cover, with surface wind speed data ~~are~~ selected from ~~the~~spatially interpolated ERA5-land hourly ~~surface~~ wind speed U and V vectors~~, which are spatially interpolated.~~. Additionally, the conversion of emissions into XCO_2 enhancements requires surface pressure and water vapor column content ~~is~~ data, which were derived from ~~the spatial and temporal interpolation of the water vapor column concentration in~~ ERA5-~~land~~Land datasets.

2.1.3 CO_2 emissions data

The power plant validation data used in this study are sourced from the Carbon Brief database (https://www.carbonbrief.org/mapped-worlds-coal-power-plants/). However, many power plants in high-latitude regions do not provide emission data. Therefore, this study also compares the results with those from Climate TRACE (https://climatetrace.org/explore/electricity-generation-co2e100-2022). Climate TRACE estimates the activity levels (capacity factors) of power plants and other facilities using satellite observations and machine learning methods. ~~This~~The database provides annual and monthly CO_2 emissions and ~~power generation capacities~~generating capacity for ~~over~~more than 500 power plants worldwide. We also compared the emissions of Climate TRACE's top 30 power plants with Carbon Brief, which had an average deviation of 9.2 %, and we considered their results to be reliable.

2.2 Emission inversion and Emission Uncertainties

Gaussian plume models are widely used for monitoring point source emissions due to their stability (Brusca et al., 2016). This study applies this method to spaceborne IPDA lidar to estimate CO_2 emissions from power plants. The basic equation of the model is as follows (~~Bovensmann~~Pasquill et al., ~~2010~~1983):

$$\Delta Q(x,y) = \frac{F}{\sqrt{2\pi}a \cdot \left(\frac{x}{x_0}\right)^{0.894} \mu} e^{-\frac{1}{2}\left(\frac{y}{a \cdot \left(\frac{x}{x_0}\right)^{0.894}}\right)^2} \tag{1}$$

$$\Delta Q(x,y) = \frac{F}{\sqrt{2\pi} \cdot \left(\frac{x}{x_0}\right)^{0.894} \mu} e^{-\frac{1}{2}\left(\frac{y}{a \cdot \left(\frac{x}{x_0}\right)^{0.894}}\right)^2} \tag{2}$$

Where x and y represent the distances from the chimney along the wind direction and vertical to the wind direction (m), ΔQ is the total CO_2 column increment (g m^{-2}), F is the point source CO_2 emission rate (g s^{-1}), and a is the atmospheric stability parameter, which is related to the solar radiation index and surface wind speed. The solar radiation index can be assessed using high cloud cover, low cloud cover, and solar elevation angle (Pasquill, 1961; Beals, 1971). The total CO_2 column amount converted to the increment of column concentration ΔXCO_2 (ppm) can be calculated using the following equation (Zheng et al., 2020):

5

$$\Delta XCO_2(x,y) = \Delta Q(x,y) \cdot \frac{\cancel{M_{air}}}{M_{CO_2}} \cdot \frac{\cancel{g}}{P_{surf} - w \cdot g} \cdot 1000 \tag{2}$$

$$\Delta XCO_2(x,y) = \Delta Q(x,y) \cdot \frac{M_{air}}{M_{CO_2}} \cdot \frac{g}{P_{surf} - w \cdot g} \cdot 1000 \tag{3}$$

Where M_{air} is the molecular mass of dry air (g mol^{-1}), M_{CO_2} is the molecular mass of carbon dioxide (g mol^{-1}), g is the

160 acceleration due to gravity, P_{surf} is the surface pressure (Pa), and w is the water vapor column content (kg m²).

The satellite-observed XCO$_2$ results need to be converted into the CO$_2$ increment ΔXCO_2 caused by power plant emissions. The diffusion of CO$_2$ plumes can be simplified using a two-dimensional Gaussian model, where the footprint of the spaceborne lidar is tangent to the two-dimensional Gaussian plume, leading to a shape similar to a one-dimensional Gaussian distribution. It is assumed that the background CO$_2$ concentration might exhibit a small gradient linear change, and XCO$_2$ distribution is

165 considered to follow the distribution:

$$\cancel{XCO_2(x) = XCO2_b + b \cdot x + \frac{a}{\sigma\sqrt{2\pi}} e^{[-(x-\mu)^2/2\sigma^2]}} \tag{3}$$

$$XCO_2(x) = XCO2_b + B \cdot x + \frac{A}{\sigma\sqrt{2\pi}} e^{[-(x-\mu)^2/2\sigma^2]} \tag{4}$$

Where A, B, σ, μ are the parameters in the linear fit function, obtained by least squares fit, $XCO2_b + \cancel{b}B \cdot x$ is background value

of XCO$_2$, $\frac{a}{\sigma\sqrt{2\pi}} e^{[-(x-\mu)^2/2\sigma^2]} \frac{A}{\sigma\sqrt{2\pi}} e^{[-(x-\mu)^2/2\sigma^2]}$ is ΔXCO_2 caused by power plant emissions (Reuter et al., 2019).
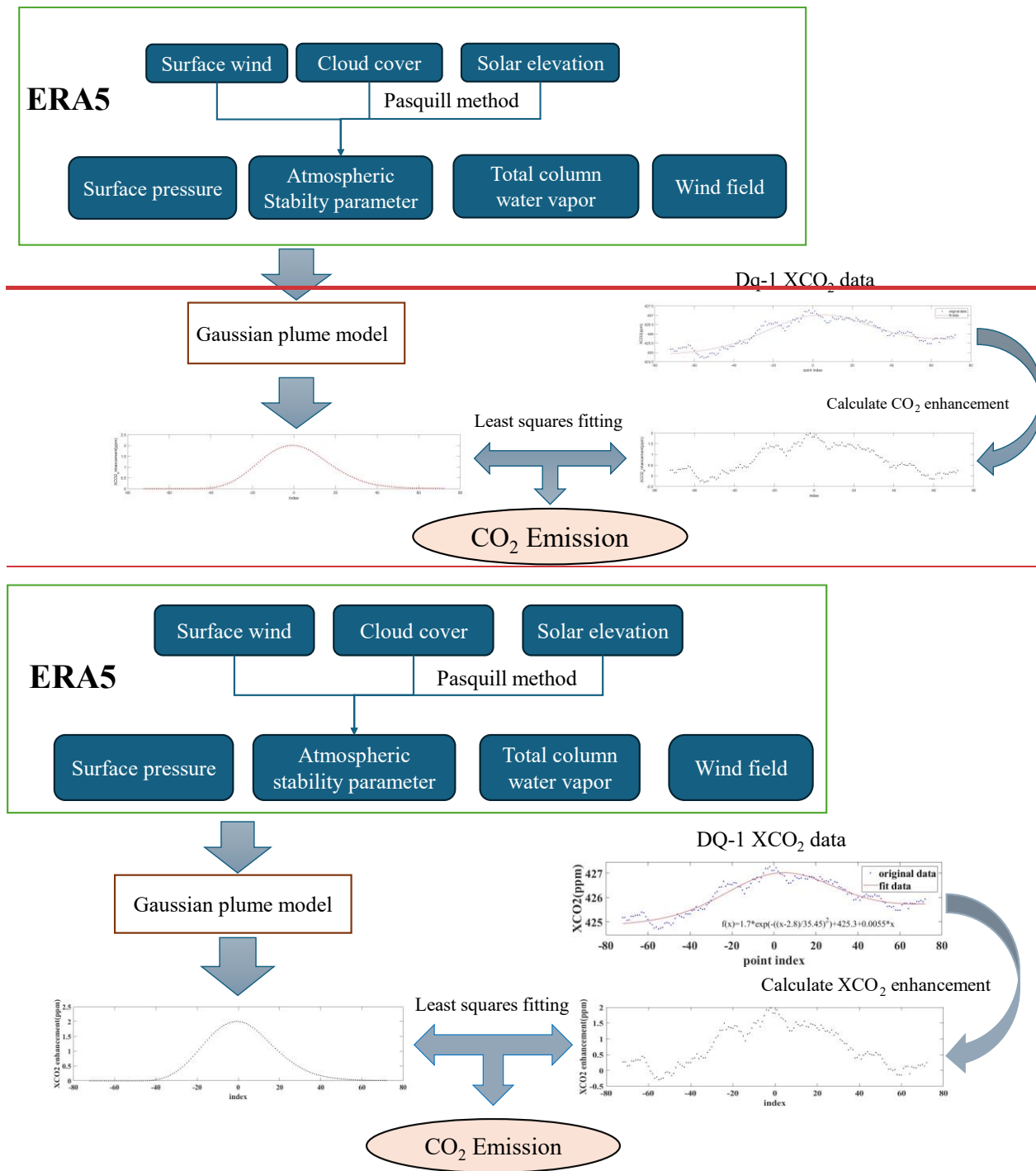
170

Figure 1: ~~inversion~~**Inversion** framework for Gaussian plume models.

The specific calculation process is illustrated in Fig. 1. ~~To~~For a power plant with an emission rate of 1000 kg s^{-1}, the downwind XCO$_2$ enhancement at 50 km under 10 m s^{-1} winds is <1 ppm, which is less than the uncertainty of XCO$_2$ observed by the DQ-1, indicating low reliability in distant plume detection. Therefore, to improve the model's fit with satellite observation results, the selected DQ-1 orbital data require that the downwind direction of the point source intersects with the satellite footprint and that the distance between the XCO$_2$ enhancement location and the point source is less than ~~30~~50 km. In the simulation, the x-axis of the Gaussian plume represents the direction of diffusion. Most studies use interpolated wind vectors from sources like ERA-5 at the plume height as the plume's direction (Guo et al., 2023). However, in practice, wind direction may deviate and change continuously, making instantaneous wind direction insufficient for accurate plume propagation. In this model, the plume propagation direction is defined as the vector from the chimney location to the centre of the Gaussian peak. This direction is then compared with the interpolated wind direction. Only results where the wind direction difference is less than 25° are selected for further comparison and validation.

The selected satellite observation results are ultimately fitted to the model's plume results at the satellite footprint using the least squares method to obtain the CO$_2$ emission rate of the target power plant. The model's results can be calculated using Eq. (~~1~~2) and (~~2~~3), where the atmospheric stability parameter significantly affects the dispersion of the plume. Direct fitting with a specific value can easily lead to estimation bias. In this study, ~~the~~ empirical interpolation of atmospheric stability ~~parameter is empirically interpolated~~parameters was implemented by ~~considering factors such as~~accounting for surface wind speed, cloud ~~cover~~coverage, and solar ~~altitude. Then,~~elevation angle, the latter calculated from latitude and time of observation (Nassar et al., 2021). The uncertainty in the stability parameter was quantified through the uncertainty in surface wind speed measurements. Subsequently, a least-squares fitting approach was applied under the assumption that prior ~~value~~estimates of ~~the~~ atmospheric stability ~~parameter is~~parameters varied ~~by~~within one standard deviation~~, and least squares fitting is performed accordingly.~~. The optimal ~~result is~~solution was then selected as the representative atmospheric instability ~~of~~value for the target location. ~~For DQ-1 observational data, smoothing~~A 10-km moving averaging was applied to ~~improve the signal~~DQ-1 data, reducing the uncertainty of XCO$_2$ to ~~noise ratio and reduce errors~~ below 1 ppm, which facilitated the detection of enhanced XCO$_2$ signals (Zhang et al., 2023). Therefore, during the least squares fitting process, the model results are also smoothed similarly. The primary differences between the Gaussian plume model used in this study and the EMI-GATE model employed by Han et al. lie in the calculation methods for the atmospheric instability parameter, background CO$_2$ column concentration, wind speed, and wind direction. Our approach involves varying these parameters within their respective error ranges based on the original observational values, with each parameter being calculated independently to maximize the interpretability of the results.

This study estimates the uncertainty in power plant emissions using a Gaussian plume model, considering five factors: uncertainty in wind speed, uncertainty in wind direction, uncertainty in plume height, uncertainty in atmospheric stability, and uncertainty in background field. The total uncertainty can be calculated using Eq. (~~4~~5):

$$c = \sqrt{c_s^2 + c_d^2 + c_h^2 + c_a^2 + c_b^2} \tag{4}$$

8

$$\varepsilon = \sqrt{\varepsilon_s^2 + \varepsilon_d^2 + \varepsilon_h^2 + \varepsilon_a^2 + \varepsilon_b^2} \qquad (5)$$

Where ε_s represents the error caused by wind speed. This is estimated by comparing the CO_2 emissions from the target power plant using wind speeds interpolated from MERRA-2 and ERA-5 data, with the wind speed uncertainty given by the ~~difference~~standard deviation between the two predictions. ε_d represents the error caused by wind direction, calculated as the difference in CO_2 emissions using wind directions interpolated from ERA-5 versus the plume direction computed in this study. ε_h represents the error caused by the emission height of the power plant. ~~Assuming~~The plume height is equal to the stack height plus the plume lift height (Brunner et al., 2019), and if there is no information on the stack height for a specific power plant, the default ~~chimney~~stack height ~~of~~is 240 ~~meters, and considering variations among different plants, including~~m, and given the uncertainty in the plume ~~rise~~lift height, ~~scenarios with chimney~~the standard deviation of the emissions for lift heights of 160 m, 200 m, 240 m, 280 m, and 320 m ~~are~~is used to estimate the uncertainty. ε_a represents the error ~~due to~~induced by atmospheric instability~~.~~, which is quantified using surface wind speed and net radiation index. The uncertainty ~~due to atmospheric instability is calculated by assuming fluctuations of one standard deviation~~ in atmospheric ~~stability parameters~~instability is derived from the uncertainty in surface wind speed data. ε_b represents the error in calculating the CO_2 background value. This is determined by comparing the average CO_2 concentration at points upwind of the source, outside the Gaussian plume, with the background value computed using the Gaussian fitting method employed in this study, thus providing the uncertainty in the CO_2 background field.

3 Results and Discussion

In this study, we utilized the DQ-1 satellite's Level 2D XCO_2 data and selected power plants with characteristics such as being located at mid-to-high latitudes and having large CO_2 emissions from Climate TRACE. ~~We retrieved all~~A total of 97 satellite ~~orbits passing~~overpasses within ~~a~~50-km circular ~~area centred on the power plant chimney with a radius of 50 km, using ERA-5 wind direction data to filter the satellite orbits.~~regions centered on plant stacks were retrieved. For 10 typical coal-fired power plants, 47 ~~sets of~~ satellite ~~footprints~~overpasses intersecting the downwind direction were ~~found~~identified within the ~~power~~ plant area. ~~The~~Strict data filtering standards were applied when using the Gaussian plume model ~~was applied with stringent data filtering criteria~~, requiring ~~no~~the absence of thick clouds (DQ-1 measured elevation discrepancies from DEM <100 m) and ensuring that the deviation of the wind direction from the plume spreading direction at the point ~~source's downwind direction intersected with the satellite orbit. Under the condition~~source was less than 25°. We consider that ~~the error between~~deviations of wind direction from the plume axis of less than 25 % are mainly attributable to meteorological data uncertainties, while larger deviations ($\geq$25 %) may be due to atmospheric turbulence effects (Panofsky et al. 1984), when Gaussian plume modelling is not appropriate. After filtering, 34 % of the overpasses were discarded due to excessive differences in wind direction, and ~~plume dispersion direction was less than 25°,~~ a total of 28 ~~cases~~overpasses were finally

9

selected, including 15 nighttime ~~observations~~cases and 3 cases where the power ~~plants were~~plant was located above 60° N ~~latitude~~.

3.1 Emissions from high latitude power plants

Reftinskaya GRES (61.7° E, 57.1° N) is the largest solid fuel-fired power plant in Russia, generating electricity by burning coal. The plant emits not only CO_2 and other greenhouse gases but also large amounts of SO_2, NO_x, and other pollutants, making the monitoring of its emissions highly significant. Located in Sverdlovsk Oblast, the plant has a total installed capacity of 3,800 MW and produces 20 billion kWh of electricity annually. Climate TRACE data shows that its CO_2 emissions in 2022 were 22.7 Mt, ranking it 8th among global power plants. This plant is a major power source for the Sverdlovsk, Tyumen, Perm, and Chelyabinsk regions. The plant's Chimney No. 4, at 330 meters, is one of the tallest chimneys in the world, while the heights of the other chimneys are still uncertain. Due to the plant's high latitude, around 57° N, ~~traditional~~ passive remote sensing satellite data ~~has a low efficiency (~~are sparse (Insufficient OCO-2 ~~satellites have no valid Gaussian plume data~~overpasses were available for GPM at this plant), making it difficult to ~~observe~~estimate. However, active remote sensing methods provide high data coverage in high-latitude regions, allowing for more accurate estimates of the plant's emissions. In this study, we retrieved two years of observational data from July 2022 to July 2024, identifying a total of 27 valid satellite orbits passing over the plant, as shown in Fig. 2. Based on ERA-5 wind direction data and the XCO_2 distribution, 19 valid observations were identified, covering both daytime and nighttime during autumn/winter and spring/summer. These data enable analysis of the plant's emissions over time, with typical daytime and nighttime observation results presented in Fig. 3.
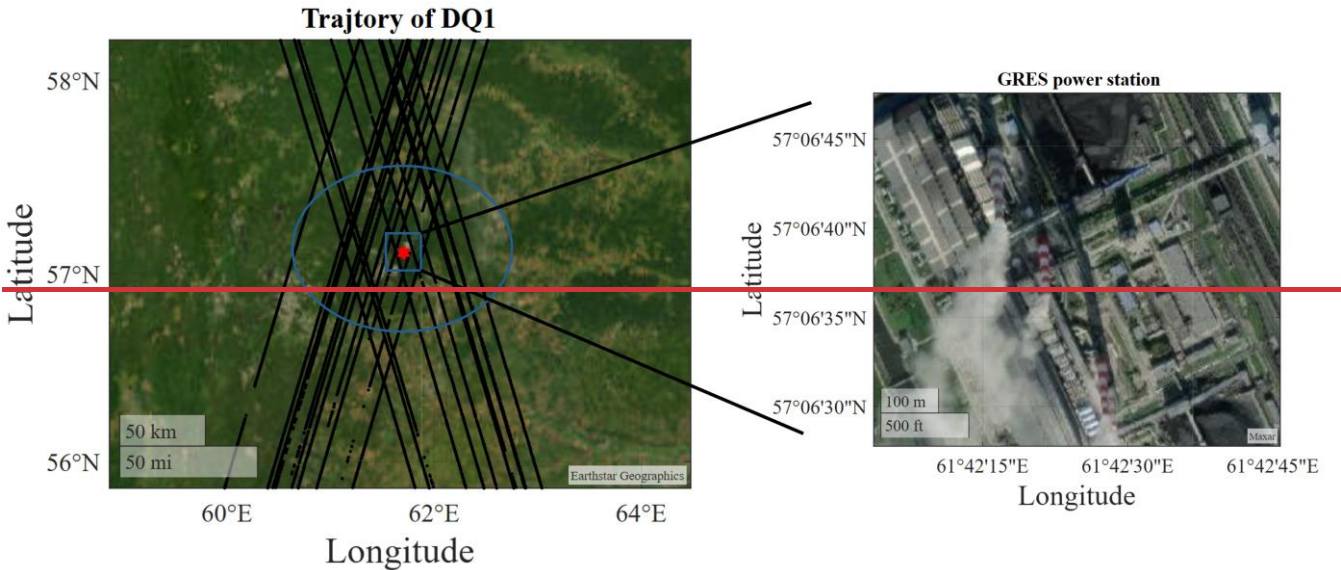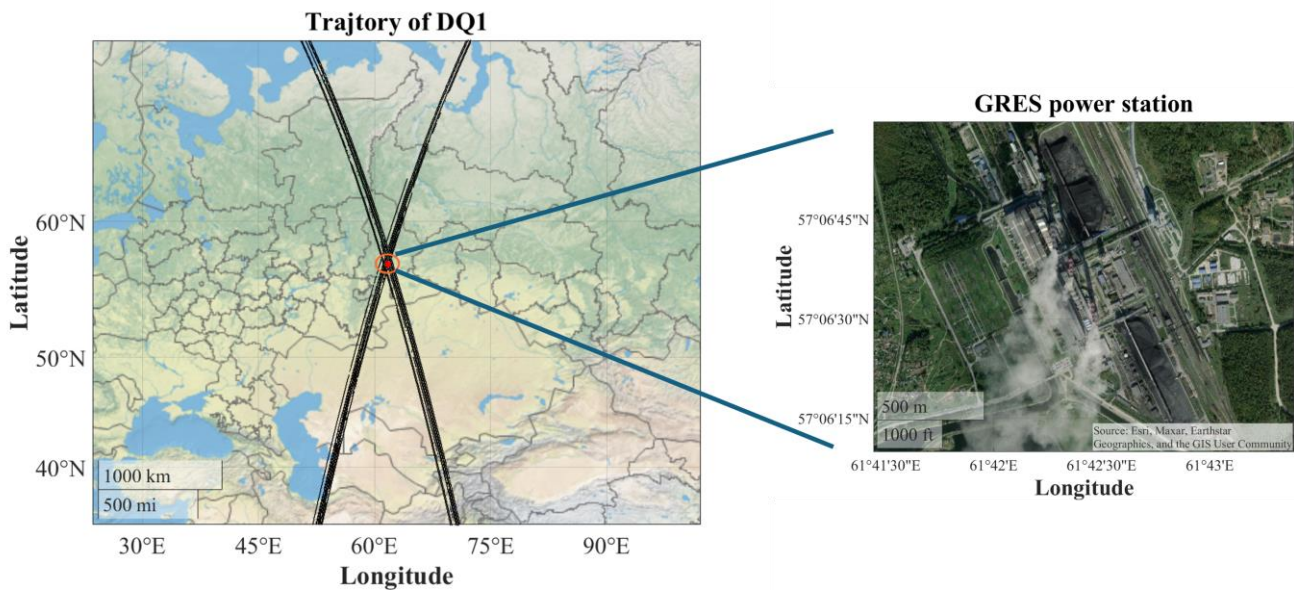
Figure 2: The DQ-1 satellite passed through all orbits around the Reftinskaya GRES power plant, where the red hexagonal star indicates the position of the power plant.
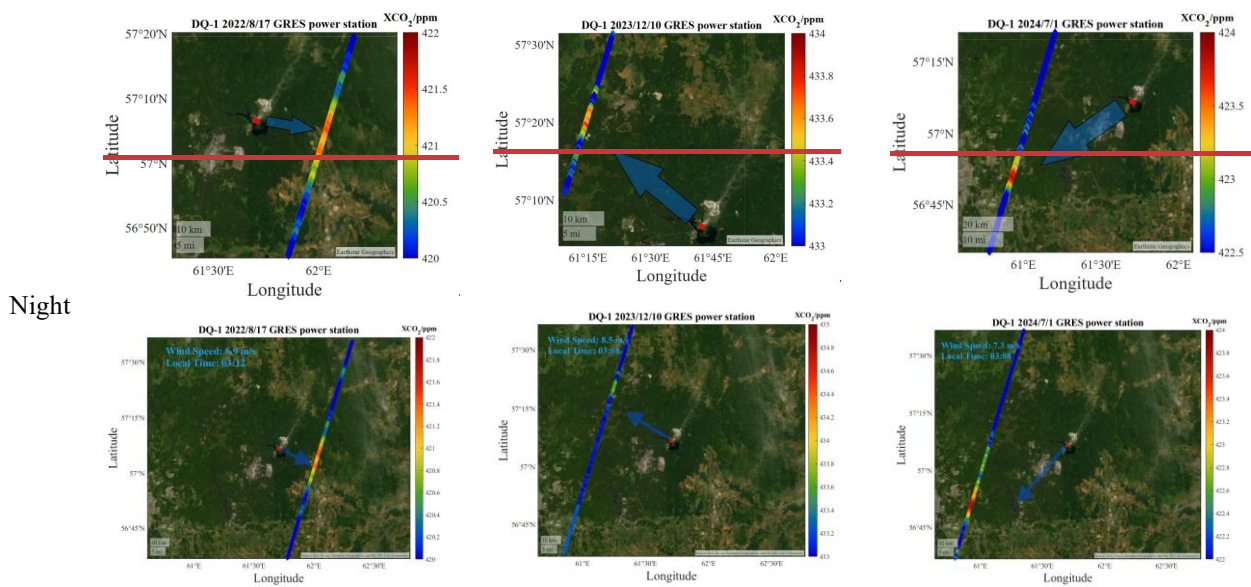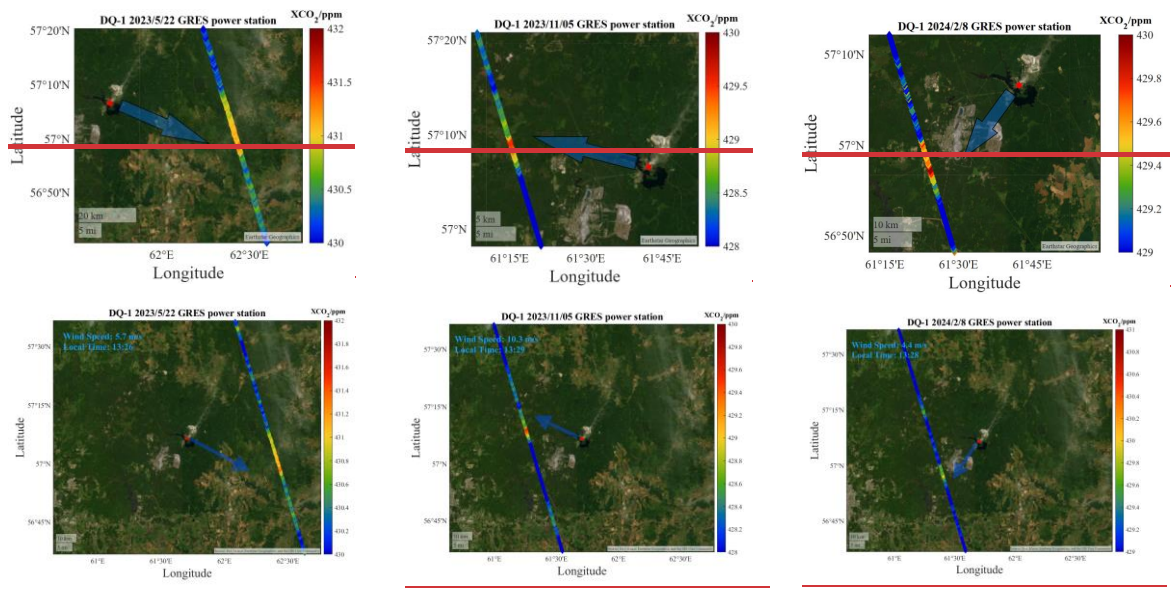

Night

Figure 3: ~~July 2022-July 2024~~Typical daytime and nighttime **DQ-1** ~~satellite passes all orbits~~overpasses **around the Reftinskaya GRES power** ~~plant, where~~station, with **the red** ~~hexagonal~~six-pointed **star** ~~indicates~~indicating **the** ~~position~~location **of the power** ~~plant~~station and the arrow representing the wind direction at the plume.

For the nighttime observation on 17 August 2022, the satellite orbit (Fig. 4a) was approximately 12 km from the power plant. Using Gaussian fitting, the background CO_2 column concentration was calculated to be 419.97 ppm, with an XCO_2 increment of about 1.3 ppm (Fig. 4b). Within the plume, there were 76 data points, assuming a plume height of 530 meters above ground level (the sum of the ~~chimney~~stack height and the assumed uplift height). The CO_2 emission rate of the inventory is 721.3 kg s^{-1}. Combined with the two-dimensional Gaussian model, the theoretical XCO_2 enhancement results were calculated (as shown in Fig. 4c), and using the least squares method, the fitted CO_2 emission result was 806.0 ± 108.2 kg s^{-1}, with a correlation coefficient of R = 0.88 (Fig. 4d). The average deviation between the model results and satellite-measured data was 0.32 ppm. The total relative error of 13.4 %, which included an uncertainty of 70.5 kg s^{-1} due to wind conditions, 39.8 kg s^{-1} due to background levels, and uncertainties of 26.1 kg s^{-1} and 64.4 kg s^{-1} due to plume height and atmospheric stability, respectively. The slightly higher result from the model compared to the emissions inventory can be attributed to the fact that the emissions inventory represents annual averages. When converting these averages into instantaneous emission rates, the result tends to be lower than the actual instantaneous emission due to shutdowns for maintenance throughout the year. ~~Although~~In mild summers, despite reduced nighttime electricity demand ~~decreases at night in the mild summer climate,~~ and ~~the power plant's~~plant output ~~is reduced, lower operational,~~ low-load operations impair combustion efficiency ~~at low loads can lead to incomplete~~, increasing fuel ~~combustion, resulting in overall CO₂~~use per kWh and exacerbating CO_2 emissions ~~slightly exceeding the emissions inventory~~through frequent start-stop cycles (Hendriks, 2012).
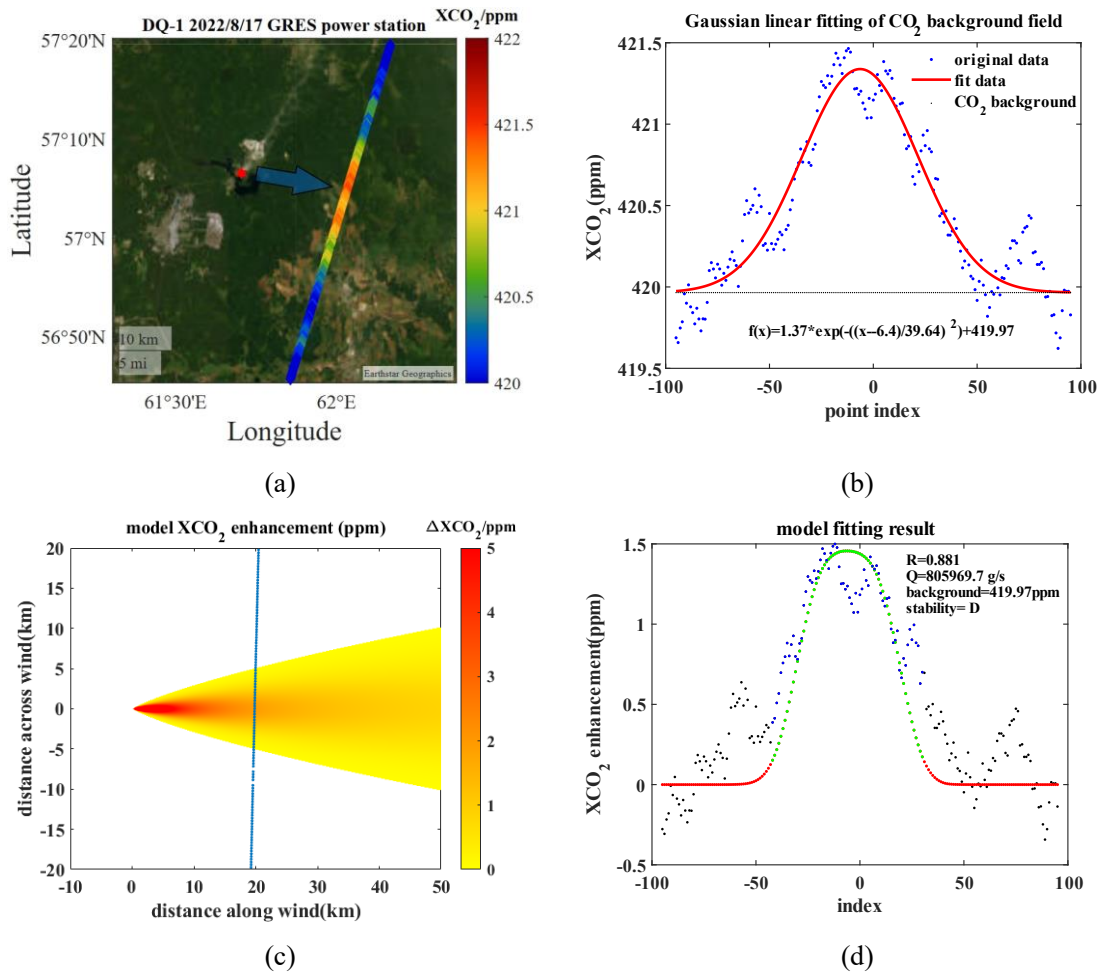
(a)

(b)

(c)

(d)

Figure 4: (a) DQ-1 satellite observation on 17 August 2022, where the red six-pointed star indicates the location of the power plant, and the red arrow indicates the result of wind interpolation of the height of the smoke plume at that location. (b)The result of one-dimensional linear Gaussian fitting of the satellite observation of XCO_2 results, the red line is the fitted result. (c) Gaussian plume distribution corresponding to the emission results calculated by the model, the blue point is the position of the satellite through the plume. (d) Comparison between the XCO_2 enhancement results fitted by the model and the measured results, with the red and green points indicating the model results, where the green points are the parts contained in the plume, and the black and blue points are the measured results of the satellites, and the blue points are the points in the plume.

On the night of 10 December 2023, the satellite also passed over this power plant, with the corresponding satellite trajectory (Fig. 5a) located about 31 km from the plant. Using Gaussian fitting, the background value was determined to be 432.42 ppm, and the XCO_2 enhancement was 1.2 ppm. There were 57 points within the Gaussian plume, and the Gaussian plume model predicted the instantaneous emission rate of the plant to be 1027.5 ± 177 kg s^{-1}, with a correlation coefficient R = 0.87. During the error calculation, the wind speeds from ERA-5 and MERRA-2 were 6.9 m s^{-1} and 7.8 m s^{-1}, respectively, contributing an uncertainty of 110.6 kg s^{-1} due to wind conditions. Additionally, the atmospheric stability was calculated to be category D, leading to an emissions uncertainty of 94.4 kg s^{-1}. Considering all factors, the total relative error was 17.3 %. Since December

13

is already winter in Russia, the increased electricity demand for city lighting, transportation, and residential heating appliances (Savić et al., 2014) required the plant to maintain higher power output to meet the surrounding cities' electricity needs, leading to an increase in instantaneous emissions.
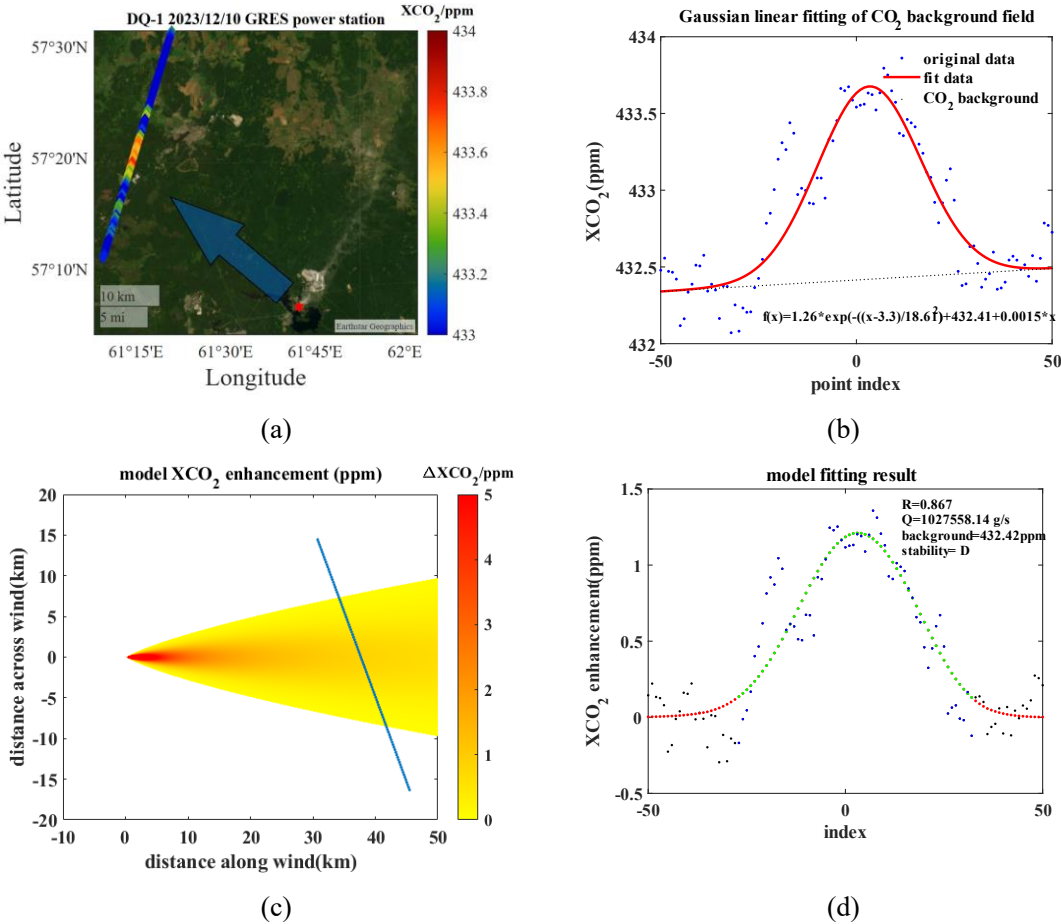

(a)

(b)

(c)

(d)

295

Figure 5: (a) Observations from the DQ-1 satellite on 20 December 2023. (b)The result after fitting the satellite observation of XCO₂ results to a one-dimensional linear Gaussian, the red line is the fitted result. (c) Gaussian plume distribution corresponding to the emission results calculated by the model (d) Comparison of the model-fitted XCO₂ enhancement results with the observation results.

On 8 February 2024, the DQ-1 satellite passed over the power plant again during the day at 08:29 UTC (Fig. 6a), with the Gaussian plume center located about 21 km downstream of the wind direction. In this observation, the atmospheric background field exhibited a strong linear variation trend, (About 0.015 ppm per kilometer along the track), and the Gaussian linear fitting results are shown in Fig. 6b, with an average XCO₂ background concentration of 428.9 ppm. The surface wind speed was 4.2 m s⁻¹, and the atmospheric stability was calculated to be class B. There were 51 points within the plume. Using the Gaussian plume model, the plant's instantaneous emission rates was predicted to be 1109 ± 169 kg s⁻¹, with a correlation coefficient R = 0.875 between the model results and satellite observations. The total uncertainty in the estimated emission rates was 168.9

14

kg s^{-1}, with a relative error of 15.3 %. The largest contribution to this uncertainty was from the variation in the CO_2 background field, which caused an emission calculation uncertainty of 109.3 kg s^{-1}. The uncertainties due to wind field, plume height, and atmospheric stability were 88.9 kg s^{-1}, 31.5 kg s^{-1}, and 85.4 kg s^{-1}, respectively. Compared to the observation in December, the CO_2 emissions were higher in this February observation, which can be attributed to the fact that the observation was conducted

310 during the day when electricity demand is higher due to residents' work activities, leading the power plant to increase output, thereby raising CO_2 emissions (Waite et al., 2017).

(a)

(b)

(c)

(d)
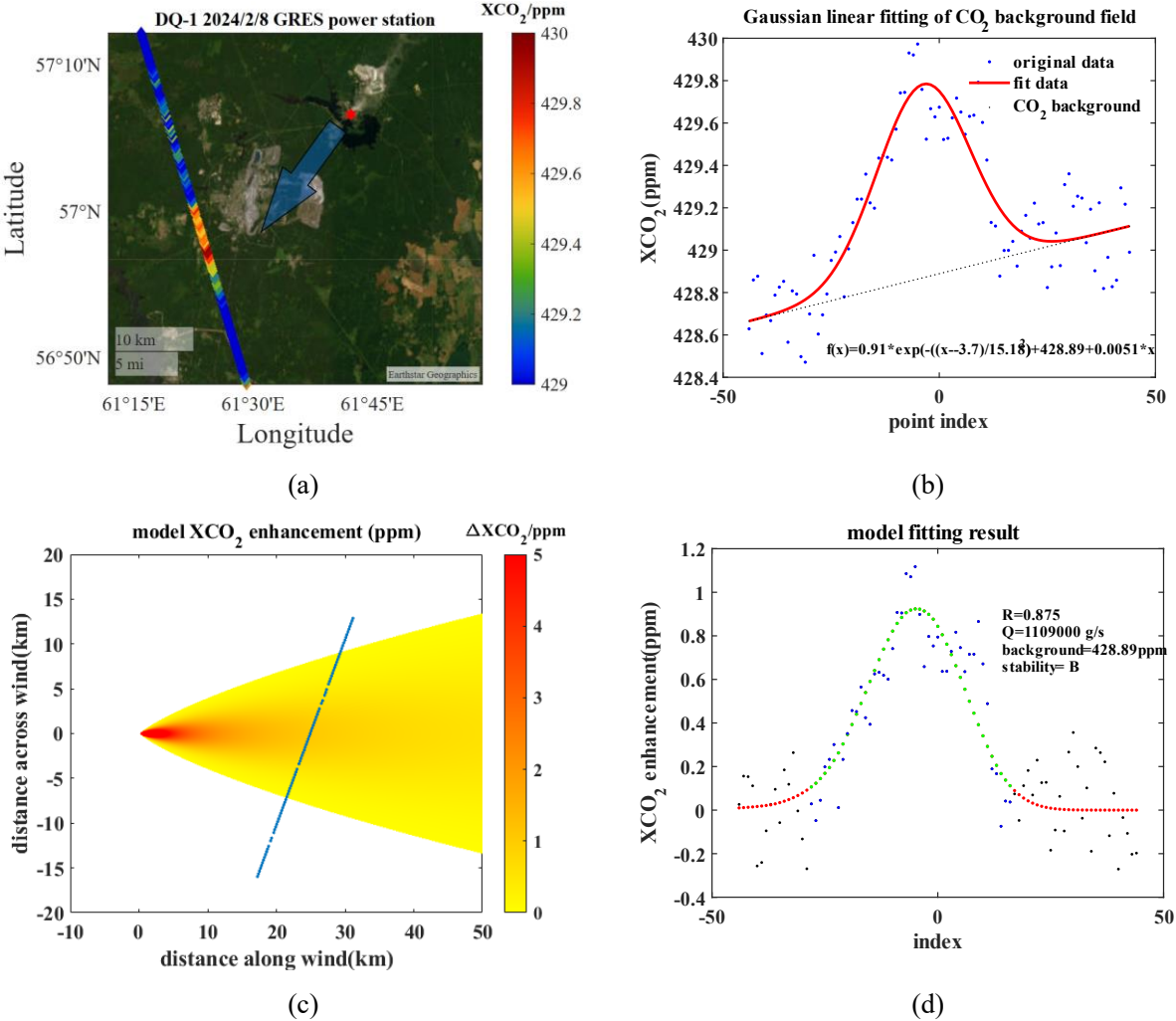
Figure 6: (a) Observations from the DQ-1 satellite on 8 February 2024. (b)Fitting the satellite observation of XCO₂ results to a one-dimensional linear Gaussian, the red line is the fitted result. (c) Gaussian plume distribution corresponding to the CO_2 emissions

315 calculated by the model (d) Comparison between the XCO₂ enhancement results fitted by the model and the measured results.

By analyzing two years of observation data from the GRES power plant (as shown in Fig. 7 and Table 1), the overall estimated average emission rate is higher than the emissions reported in the inventory. The plant undergoes annual shutdowns for

15

maintenance, and the satellite observations represent instantaneous emissions, which may differ slightly from the annual average emissions. Additionally, the Climate TRACE data reflects the 2022 annual average emissions, and the plant's yearly

320 emissions fluctuate due to varying local electricity demand. Fig. 7 shows that summer emissions are lower than winter emissions. It was found that the plant is located in a high-latitude region where the climate is mild in summer and cold in winter. During winter, residents use electrical appliances and heating systems more frequently, and the power demand for urban infrastructure is higher than in summer. As a result, the power plant adjusts its output, leading to higher CO_2 emissions in winter (Savić et al., 2014). The comparison between daytime and nighttime observations shows that the average CO_2

325 emission rate during the day is 1022 kg s^{-1}, while the nighttime average is 796 kg s^{-1}. The ratio of daytime to nighttime emission rates is 1.28. This ratio can be used to estimate the full-day CO_2 emissions when only daytime or nighttime observations are available. The power plant is the primary source of electricity for the region, and electricity demand from production activities during the day is much higher than at night. Consequently, the plant increases its load during the day, resulting in higher CO_2 emissions. This also indicates that the plant does not engage in unauthorized nighttime emissions during the observation period.
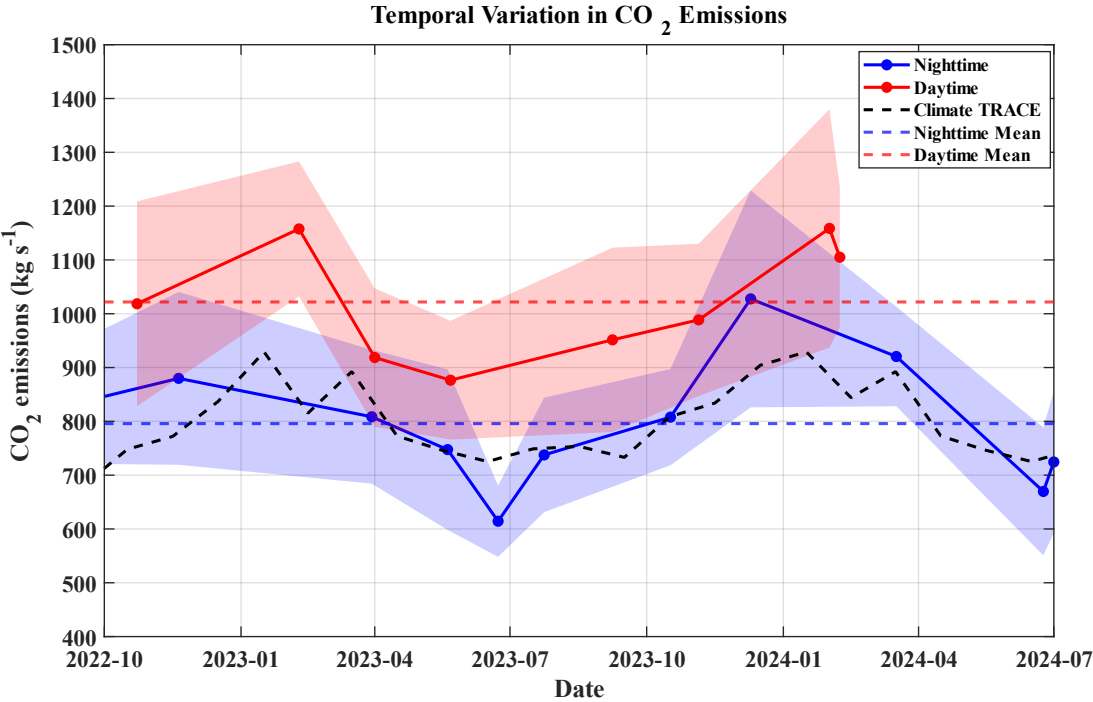
330

Figure 7: Daytime (red) and nighttime (blue) CO_2 emission rates from GRES power plants (2022–2024). Solid lines represent modeled estimates with uncertainty bounds (shaded areas); red and blue dashed lines represent average daytime and nighttime emissions, and black dashed lines represent Climate TRACE emission inventory values.

Table 1 Emission estimates and uncertainty for GRES power plant

Date	Day or Night	Estimated emissions (kg s^{-1})	Climate TRACE (kg s^{-1})	Estimated Uncertainty (kg s^{-1})

16

2022-08-17	Night	966	697.1	156.5
2022-10-23	Day	1018.5	748.1	186.9
2022-11-20	Night	1029.9	772	150.8
2023-02-09	Day	1157.6	815.2	153.1
2023-03-30	Night	958.5	892.4	130.9
2023-04-01	Day	918.6	772.8	142.6
2023-05-20	Night	897.5	746.1	100.4
2023-05-22	Day	876.5	746.1	173.5
2023-06-23	Night	764.4	725.3	118.9
2023-07-24	Night	887.6	748.8	83.0
2023-09-08	Day	951.5	733	147.4
2023-10-17	Night	957.8	808.6	139.8
2023-11-05	Day	988.6	834.1	131.5
2023-12-10	Night	1177.6	904.3	169.2
2024-02-01	Day	1158.6	844.1	187.6
2024-02-08	Day	1105	844.1	150.4
2024-03-17	Night	1070.5	892.4	168.7
2024-06-24	Night	819.7	725.3	93.6
2024-07-01	Night	874.5	748.8	126.8

335

3.2 Comparison with emission inventories

The estimations from this study were compared with the emission inventories provided by Climate TRACE and Carbon Brief, as shown in Table 2. Both inventories present the annual total emission values, whereas the model results calculated from satellite observations represent instantaneous emission rates. Due to the power plant's ability to adjust its output based on local

340 electricity demand, some differences between the two sets of results are expected. However, most results fall within the error range of the model predictions. The study includes three observation cases for latitude above 60° N and 15 cases of night-time emission detections. The use of spaceborne lidar to detect XCO_2 effectively compensates for the limitations of passive remote sensing satellites in high-latitude and night-time observations. A comparison of all observation results with the Climate TRACE inventory is shown in Fig. 8, with a correlation coefficient of 0.97.

345 **Table 2 Information on different power plants and the comparison of model predictions with emission inventories**

Country	Station	Stack Height (m)	Latitude	UTC Time	Model Result (kg s^{-1})	Climate TRACE (kg s^{-1})	Carbon Brief (kg s^{-1})	Day or Night

| Russia	GRES	330	57.11° N	2022/8/17 22:12	806.0±108	721.3	638	Night
Russia	GRES	330	57.11° N	2023/5/22 08:35	876.2 ±153	721.3	638	Day
Russia	GRES	330	57.11° N	2023/11/05 22:10	988.6±161	721.3	638	Night
Russia	GRES	330	57.11° N	2023/12/10 22:08	1027.5±177	721.3	638	Night
Russia	GRES	330	57.11° N	2024/2/8 08:29	1109±169	721.3	638	Day
Russia	GRES	330	57.11° N	2024/7/1 22:08	724.5±115	721.3	638	Night
America	Scherer	305	33.06° N	2022/5/3 02:37	478±72	267.4	607.5	Night
Poland	Belchatow	300	51.26° N	2022/5/8 19:18	771±134	867.5	925	Day
South Africa	Medupi	240*	23.71° S	2022/7/24 07:21	598±98	516.6	515.3	Day
South Africa	Matimba	240*	23.60° S	2022/7/24 07:21	708±118	617	664.6	Day
Russia	CHP-1	240*	69.33° N	2022/6/14 21:07	109.7±18	83	--	Night
Russia	CHP-3	240*	69.32° N	2022/6/14 21:07	57.1±12	44.1	--	Night
Russia	GRES-2	420	61.28° N	2022/7/24 21:36	1287.3±143	1001.1	--	Night
Korean	Taean	240*	36.90° N	2022/6/03 04:44	991.5±73	1022.2	900.5	Day
Korean	Daesan	240*	36.99° N	2022/6/03 04:44	30.4±3.4	23.9	--	Day
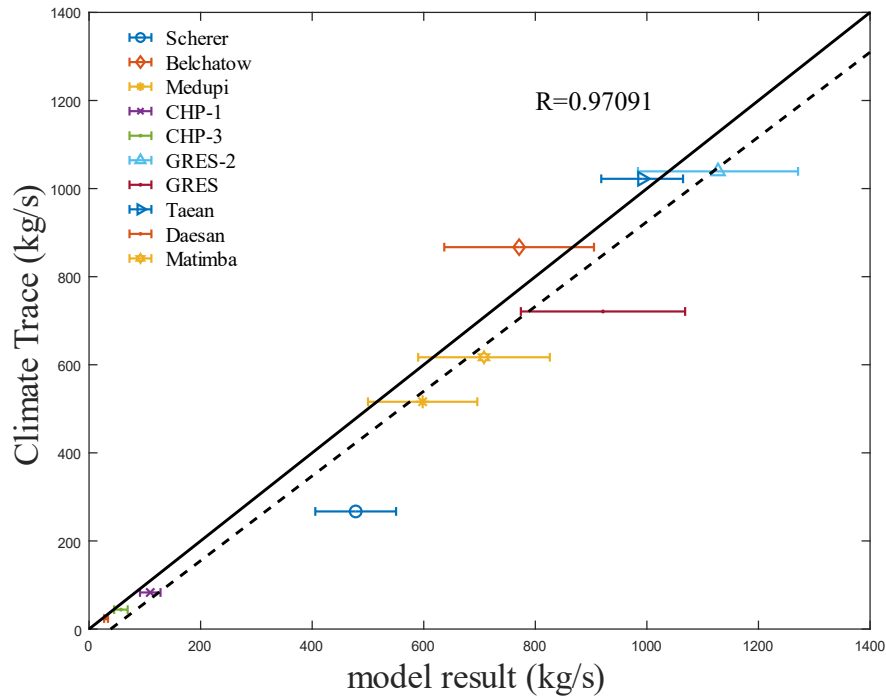
Figure 8: Comparison of power plant emissions predicted by Gaussian plume model with Climate TRACE statistics, the solid black line represents the 1:1 line, and the dashed line indicates the linear fitting line.

350 Overall, the CO_2 emissions predicted by the Gaussian plume model are generally higher than those in the emissions inventory. This discrepancy may be due to the timing of observations, as some were conducted during winter and summer in the Northern Hemisphere when increased electricity demand prompts power plants to elevate generation capacity. Comparisons between nighttime and daytime CO_2 emissions reveal lower nighttime emissions at some plants, potentially attributable to reduced electricity demand (Waite et al., 2017) and real-time adjustments to avoid power storage saturation. However, nighttime

355 emissions at certain plants exceed inventory values, which could result from suboptimal equipment load levels reducing overall efficiency and causing incomplete fuel combustion. Additionally, frequent start-stop operations during low-load conditions may contribute to unstable combustion, further amplifying emissions (Hendriks, 2012). Overall, Quantify the higher emission rates vs. Carbon Brief and Climate TRACE, a difference that might arise because conventional power plants undergo annual shutdowns for inspections, lowering annual averages relative to instantaneous emissions. It is critical to acknowledge that

360 direct validation against stack monitor measurements is unavailable, and emission inventories are inherently uncertain and not independently validated. Therefore, comparisons between estimated results and inventories should be interpreted cautiously and serve as a provisional reference rather than definitive conclusions. Moreover, by utilizing the high spatial resolution of the
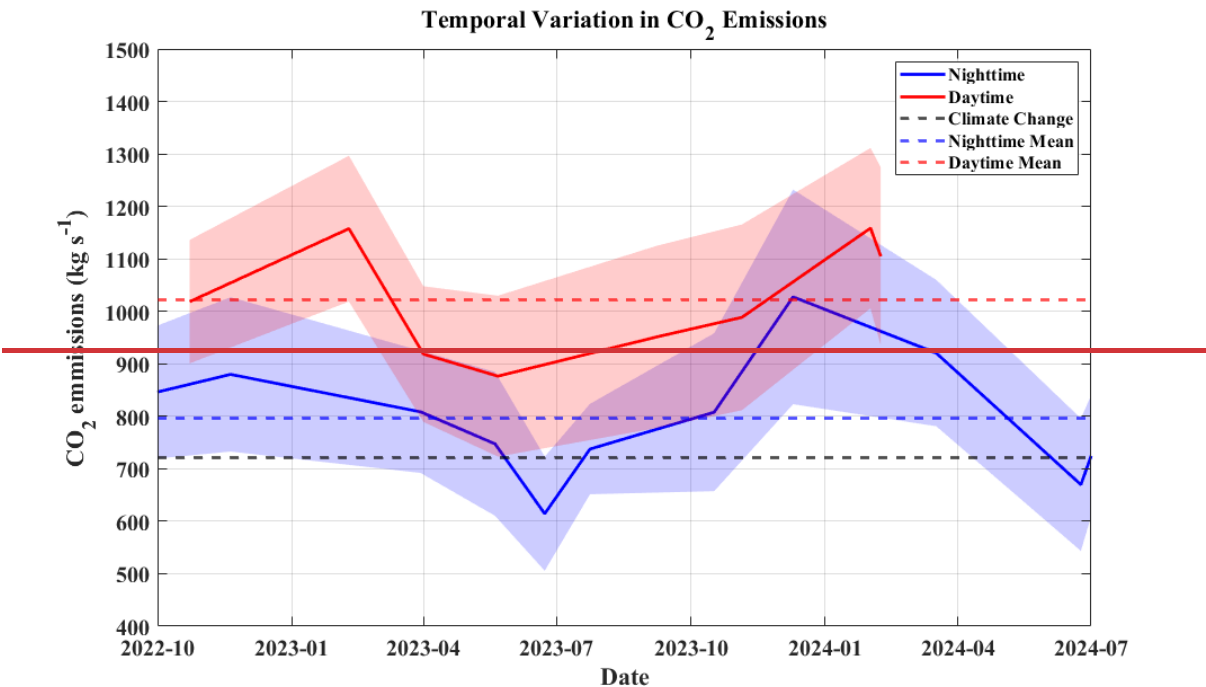
Figure 7: Diurnal emission rates of CO_2 from the GRES power plant over a 2-year period, with daytime results in red and nighttime observations in blue

3.23.3 Emissions uncertainty analysis

The uncertainty in the model calculations was assessed using Eq. (45) from Sect. 2.2, revealing that the uncertainty contributions vary across different power plants and influencing factors. The overall uncertainty results are presented in Table 13. The average relative random error is 15.11 %, which is lower than the 18.8 % random error of the EMI-GATE model (Han et al., 2024). The primary contributors to this uncertainty are errors in the background field calculation, wind field errors, and atmospheric stability errors. Regarding wind fields, both the ERA-5 and MERRA-2 datasets are reanalysis results However, discrepancies can occur between these datasets, particularly in high-latitude regions where wind speed observations are sparse. When these wind speeds are used in the Gaussian model to estimate power plant emissions, differences can lead to errors in Gaussian diffusion velocity, thereby affecting prediction accuracy (Nassar et al., 2021). In this study, wind field-related uncertainty accounts for 26.7 % of the total error, with an average relative random error of 7.4 %. Atmospheric stability is another significant factor contributing to uncertainty. Atmospheric stability is not constant and varies in real-time with solar radiation, which is influenced by factors such as cloud cover and solar elevation angle (Ashrafi and Hoshyaripour, 2010). Since atmospheric stability directly impacts the shape of Gaussian diffusion, it introduces errors in predicted CO_2 emissions. For all results considered, uncertainty due to atmospheric stability contributes 25.1 % to the total error, with an average relative

random error of 7.3 %. Plume height uncertainty also plays a role in the overall error. While some power plants provide chimney height data, allowing for the consideration of plume rise uncertainty only, others require an assumed chimney height (Guo et al., 2023). This assumption can lead to relatively high errors, primarily because wind speed and direction near the ground can vary with height, resulting in inaccuracies in wind field calculations. Plume height uncertainty contributes 6.5 % to the total error, with an average relative random error of 3.3 %. Uncertainty in the background field is mainly due to inaccuracies in its calculation. In areas with significant anthropogenic interference, a linear function may not adequately represent changes in background CO_2 concentration. ~~Although the XCO₂ observation accuracy of the DQ-1~~Additionally, satellite ~~is better than 1 ppm, uncertainty in its results contributes~~observations are subject to inherent errors ~~in~~, and uncertainties in XCO_2 retrievals can introduce errors into point-source emission estimation. Background field errors account for 40.7 % of the total error, with an average relative random error of 9.5 %. For spaceborne lidar, the spatial distribution of satellite nadir points differs from that of passive remote sensing satellites, leading to fewer observed points within the plume. This increases the weight of background field uncertainty in the total error (Nassar et al., 2021; Shi et al., 2023). The uncertainty of XCO_2 around the studied power plants is less than 1 ppm by moving average, but the average relative error of XCO_2 enhancement at the peak of the plume is as high as 47.3%. Compared to the statistical uncertainties reported in Han et al (Han et al., 2024), both investigations identified that uncertainties in the DQ-1 satellite's XCO_2 observations dominate the error budget, accounting for approximately 50% of the total error. Beyond this, the significant contribution of wind field uncertainties aligns with findings from Nassar et al (Nassar et al., 2017; Guo et al., 2023). In contrast to previous studies, this work incorporates uncertainties in atmospheric instability. Due to the influence of turbulence and other factors within the boundary layer, the uncertainty in surface wind speed also exerts a significant influence on atmospheric instability calculations.

Table ~~1~~3 Uncertainty caused by different error factors in the forecast results of different power plants.

Power Station	Wind field (Kg s⁻¹)	Plume height (Kg s⁻¹)	Stability (Kg s⁻¹)	Background field (Kg s⁻¹)	Total error (Kg s⁻¹)	Relative error
Scherer	34.2	13.9	59.4	47.4	72.4	15.1 %
Belchatow	48.3	14.5	72.9	98.8	134.2	15.4 %
Medupi	64	45.8	12.3	52.8	98	16.4 %
Matimba	81.3	21.7	34.8	75.5	118.3	16.7 %
CHP-1	4.3	1.9	9.5	15.2	18.4	16.7 %
CHP-3	5.2	1.8	5.8	9.1	12.1	21.2 %
GRES-2	43.2	31.2	72.3	107.2	143.5	12.6 %
GRES	80.3	27.8	71.8	90.7	147.3	15.9 %
Taean	51.8	27.4	10.8	27.8	73.3	7.4 %
Daesan	2.8	0.9	1.6	1.2	3.5	12.7 %

3.3 Validation of Emission results

Unlike prior studies, this research explicitly accounts for atmospheric instability uncertainty. Surface wind speed uncertainty, influenced by boundary layer turbulence and other factors, is significantly higher during daytime. Our analysis of 28 cases reveals that the optimized atmospheric instability parameter a shows average deviations of 19.5% from its prior value in daytime versus 15.8% at night. The results indicate that, under the assumption that plume dispersion aligns with the Gaussian plume model, ERA-5 surface wind speeds exhibit higher accuracy at night. However, daytime turbulence introduces small-scale wind field errors, which further amplify uncertainties in atmospheric instability.

The estimations from this study were compared with the emission inventories provided by Climate TRACE and Carbon Brief, as shown in Table 2. Both inventories present the annual total emission values, whereas the model results calculated from satellite observations represent instantaneous emission rates. Due to the power plant's ability to adjust its output based on local electricity demand, some differences between the two sets of results are expected. However, most results fall within the error range of the model predictions. The study includes three observation cases for latitude above 60° N and 15 cases of night-time emission detections. The use of spaceborne lidar to detect XCO_2 effectively compensates for the limitations of passive remote sensing satellites in high-latitude and night-time observations. A comparison of all observation results with the Climate TRACE inventory is shown in Fig. 8, with a correlation coefficient of 0.97.

Table 2 Information on different power plants and the comparison of model predictions with emission inventories

Country	Station	Latitude	UTC Time	Model Result $(kg \cdot s^{-1})$	Climate TRACE $(kg \cdot s^{-1})$	Carbon Brief $(kg \cdot s^{-1})$	Day or Night
Russia	GRES	57.11° N	8/17 22:12	806.0±108	721.3	638	Night
Russia	GRES	57.11° N	5/22 08:35	876.2 ±153	721.3	638	Day
Russia	GRES	57.11° N	11/05 22:10	988.6±161	721.3	638	Night
Russia	GRES	57.11° N	12/10 22:08	1027.5±177	721.3	638	Night
Russia	GRES	57.11° N	2/8 08:29	1109±169	721.3	638	Day
Russia	GRES	57.11° N	7/1 22:08	724.5±115	721.3	638	Night
America	Scherer	33.06° N	5/3 02:37	478±72	267.4	607.5	Night
Poland	Belchatow	51.26° N	5/8 19:18	771±134	867.5	925	Day

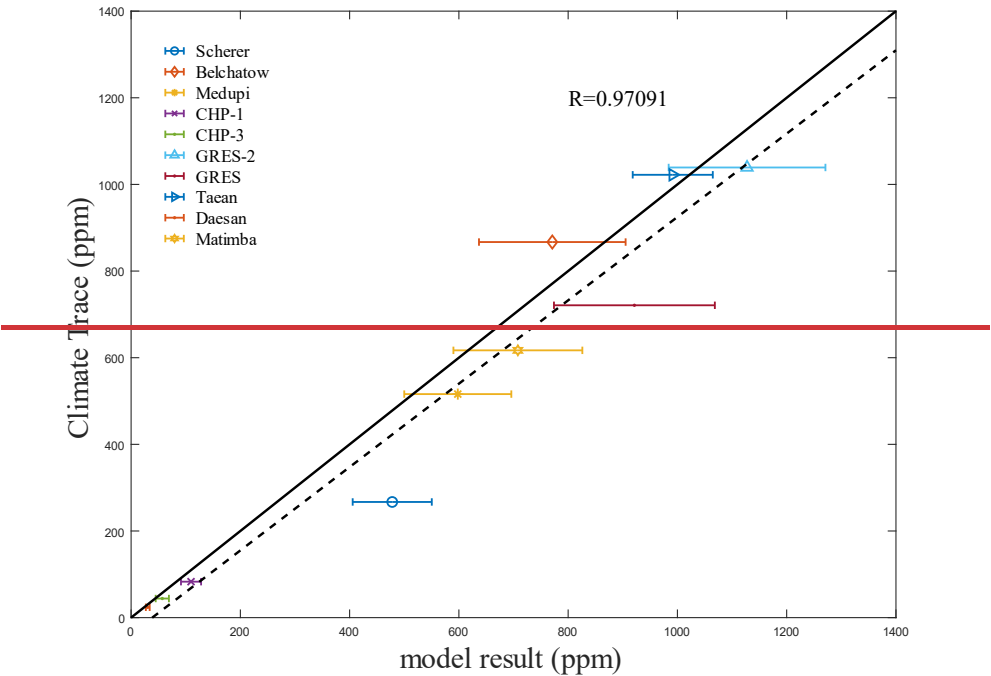|							
South Africa	Medupi	23.71° S	7/24 07:21	598±98	516.6	515.3	Day
South Africa	Matimba	23.60° S	7/24 07:21	708±118	617	664.6	Day
Russia	CHP-1	69.33° N	6/14 21:07	109.7±18	83	—	Night
Russia	CHP-3	69.32° N	6/14 21:07	57.1±12	44.1	—	Night
Russia	GRES-2	61.28° N	7/24 21:36	1287.3±143	1001.1	—	Night
Korean	Taean	36.90° N	6/03 04:44	991.5±73	1022.2	900.5	Day
Korean	Daesan	36.99° N	6/03 04:44	30.4±3.4	23.9	—	Day

Figure 8: Comparison of power plant emissions predicted by Gaussian plume model with Climate TRACE statistics, the solid black line represents the 1:1 line, and the dashed line indicates the linear fitting line.

Overall, the CO_2 emissions predicted by the Gaussian plume model are generally higher than those in the emissions inventory. This is because some of the observations were made during the winter and summer in the Northern Hemisphere when residents' demand for electricity, such as air conditioning, increases, prompting power plants to raise their generation capacity. Comparing nighttime CO_2 emissions with daytime observations shows that emissions from some power plants are lower at

420

425

23

night, primarily due to reduced electricity demand at night (Waite et al., 2017), and some power stations adjust power generation in real-time to avoid power storage saturation. However, for some plants, nighttime emissions exceed those in the inventory, possibly because when the load on the equipment is below its optimal level, the plant's overall efficiency decreases, leading to incomplete fuel combustion. Additionally, frequent start-stop operations during low-load conditions may cause unstable combustion, further increasing emissions (Hendriks, 2012). Overall, the predicted emissions are slightly higher than those reported by Carbon Brief and Climate TRACE, mainly because conventional power plants undergo annual shutdowns for equipment inspections, resulting in lower annual averages compared to instantaneous emissions. Moreover, by utilizing the high spatial resolution of the DQ-1 satellite, it is possible to monitor low CO_2-emitting power plants ($F < 100$ kg s^{-1}), with results fitting well with the inventory data.

4 Conclusions

This study utilized the IPDA lidar aboard the DQ-1 satellite to monitor emissions from localized strong point sources and, for the first time, observed the diurnal variation of CO_2 emissions from a high-latitude power plant, effectively covering areas that passive remote sensing satellites fail to monitor. The two-dimensional Gaussian plume model was optimized in terms of plume direction and atmospheric stability and applied to XCO_2 observation results. Validation and comparison results indicate that the improved Gaussian plume model has a strong correlation with the emissions inventory, with a correlation coefficient of 0.97. The average relative random error of the predicted results is 15.11 %, which is lower than that of the EMI-GATE model, due to different parameter selections in the Gaussian plume model, thus reducing the random error. The main factors affecting estimation errors are the uncertainty in the atmospheric wind field (26.7 % of total error), uncertainty in atmospheric stability (25.1 %), and uncertainty in background field calculations (40.7 %). The results show that during the daytime, the error in the surface wind field is higher due to turbulence, which can cause some invalid observations or increase the error caused by atmospheric instability and wind field to the model. Utilizing high-resolution wind fields simulated by the WRF-LES model around power plants to drive the Gaussian plume model may reduce uncertainties in wind field. Establishing automatic weather stations around the power plant for real-time monitoring of atmospheric radiation and surface wind speed could reduce errors caused by uncertainties in atmospheric stability. Overall, power plant CO_2 emissions were largely consistent with local electricity consumption patterns, with most plants emitting less at night than during the day, and with higher emissions in winter and summer compared to spring and autumn. This research provides a new approach for global carbon accounting. In 2025, China will launch the DQ-2 satellite, equipped with the same IPDA lidar for carbon dioxide observation. As satellite density increases, global coverage of emissions detection data will significantly improve.

Data availability.

ERA-5: https://cds.climate.copernicus.eu/#!/home.

MERRA-2: https://gmao.gsfc.nasa.gov/reanalysis/MERRA-2/

Carbon brief: https://www.carbonbrief.org/mapped-worlds-coal-power-plants/

Climate TRACE: https://climatetrace.org/explore/electricity-generation-co2e100-2022

460 ACDL: The ACDL dataset is under restricted access, the data can be requested at https://data.cresda.cn/#/home

Author contributions.

XZ, HY and LB designed and directed the study. XZ and ZF contributed to data analysis and wrote the first draft of this paper. BC, LZ, SL, ZW and WC collected data. JL, XL and WX contributed the data interpretation and review of the paper.

Competing interests.

465 The authors declared that they have no conflict of interest.

Disclaimer.

Publisher's note: Copernicus Publications remains neutral with regard to jurisdictional claims made in the text, published maps, institutional affiliations, or any other geographical representation in this paper. While Copernicus Publications makes every effort to include appropriate place names, the final responsibility lies with the authors.

References

Ahn, D., Hansford, J. R., Howe, S. T., Ren, X. R., Salawitch, R. J., Zeng, N., Cohen, M. D., Stunder, B., Salmon, O. E., and Shepson, P. B.: Fluxes of atmospheric greenhouse-gases in Maryland (FLAGG-MD): Emissions of carbon dioxide in the Baltimore, MD-Washington, DC area, Journal of Geophysical Research: Atmospheres, 125, e2019JD032004, 2020.

Amediek, A., Ehret, G., Fix, A., Wirth, M., Büdenbender, C., Quatrevalet, M., Kiemle, C., and Gerbig, C.: CHARM-F—a new airborne integrated-path differential-absorption lidar for carbon dioxide and methane observations: measurement performance and quantification of strong point source emissions, Applied Optics, 56, 5182-5197, 2017.

Arias, P., Bellouin, N., Coppola, E., Jones, R., Krinner, G., Marotzke, J., Naik, V., Palmer, M., Plattner, G.-K., and Rogelj, J.: Climate Change 2021: the physical science basis. Contribution of Working Group I to the Sixth Assessment Report of the Intergovernmental Panel on Climate Change; technical summary, 2021.

Ashrafi, K. and Hoshyaripour, G. A.: A model to determine atmospheric stability and its correlation with CO concentration, International Journal of Civil and Environmental Engineering, 2, 82-88, 2010.

Beals, G. A.: Guide to local diffusion of air pollutants, Air Weather Service (MAC), US Air Force 1971.

Bovensmann, H., Buchwitz, M., Burrows, J., Reuter, M., Krings, T., Gerilowski, K., Schneising, O., Heymann, J., Tretner, A., and Erzinger, J.: A remote sensing technique for global monitoring of power plant CO 2 emissions from space and related applications, Atmospheric Measurement Techniques, 3, 781-811, 2010.

Brusca, S., Famoso, F., Lanzafame, R., Mauro, S., Garrano, A. M. C., and Monforte, P.: Theoretical and experimental study of Gaussian Plume model in small scale system, Energy Procedia, 101, 58-65, 2016.

Brunner, D., Kuhlmann, G., Marshall, J., Clément, V., Fuhrer, O., Broquet, G., Löscher, A., and Meijer, Y.: Accounting for the vertical distribution of emissions in atmospheric CO 2 simulations, Atmospheric Chemistry and Physics, 19, 4541-4559, 2019.

Brunner, D., Kuhlmann, G., Henne, S., Koene, E., Kern, B., Wolff, S., Voigt, C., Jöckel, P., Kiemle, C., and Roiger, A.: Evaluation of simulated CO 2 power plant plumes from six high-resolution atmospheric transport models, Atmospheric Chemistry and Physics, 23, 2699-2728, 2023.

Cai, M., Han, G., Ma, X., Pei, Z., and Gong, W.: Active–passive collaborative approach for XCO 2 retrieval using spaceborne sensors, Optics Letters, 47, 4211-4214, 2022.

Crisp, D., Pollock, H. R., Rosenberg, R., Chapsky, L., Lee, R. A., Oyafuso, F. A., Frankenberg, C., O'Dell, C. W., Bruegge, C. J., and Doran, G. B.: The on-orbit performance of the Orbiting Carbon Observatory-2 (OCO-2) instrument and its radiometrically calibrated products, Atmospheric Measurement Techniques, 10, 59-81, 2017.

Ehret, G., Kiemle, C., Wirth, M., Amediek, A., Fix, A., and Houweling, S.: Space-borne remote sensing of CO 2, CH 4, and N 2 O by integrated path differential absorption lidar: a sensitivity analysis, Applied Physics B, 90, 593-608, 2008.

Eldering, A., Taylor, T. E., O'Dell, C. W., and Pavlick, R.: The OCO-3 mission: measurement objectives and expected performance based on 1 year of simulated data, Atmospheric Measurement Techniques, 12, 2341-2370, 2019.

Fan, C., Chen, C., Liu, J., Xie, Y., Li, K., Zhu, X., Zhang, L., Cao, X., Han, G., and Huang, Y.: Preliminary analysis of global column-averaged CO_2 concentration data from the spaceborne aerosol and carbon dioxide detection lidar onboard AEMS, Optics Express, 32, 21870-21886, 2024.

Friedlingstein, P., O'sullivan, M., Jones, M. W., Andrew, R. M., Gregor, L., Hauck, J., Le Quéré, C., Luijkx, I. T., Olsen, A., and Peters, G. P.: Global carbon budget 2022, Earth System Science Data, 14, 4811-4900, 2022.

Gelaro, R., McCarty, W., Suárez, M. J., Todling, R., Molod, A., Takacs, L., Randles, C. A., Darmenov, A., Bosilovich, M. G., and Reichle, R.: The modern-era retrospective analysis for research and applications, version 2 (MERRA-2), Journal of climate, 30, 5419-5454, 2017.

Guo, W., Shi, Y., Liu, Y., and Su, M.: CO2 emissions retrieval from coal-fired power plants based on OCO-2/3 satellite observations and a Gaussian plume model, Journal of Cleaner Production, 397, 136525, 2023.

Gurney, K. R., Liang, J., Patarasuk, R., O'Keeffe, D., Huang, J., Hutchins, M., Lauvaux, T., Turnbull, J. C., and Shepson, P. B.: Reconciling the differences between a bottom-up and inverse-estimated FFCO2 emissions estimate in a large US urban area, Elem Sci Anth, 5, 44, 2017.

Han, G., Huang, Y., Shi, T., Zhang, H., Li, S., Zhang, H., Chen, W., Liu, J., and Gong, W.: Quantifying CO2 emissions of power plants with Aerosols and Carbon Dioxide Lidar onboard DQ-1, Remote Sensing of Environment, 313, 114368, 2024.

Hendriks, C.: Carbon dioxide removal from coal-fired power plants, Springer Science & Business Media2012.

Hersbach, H., Bell, B., Berrisford, P., Hirahara, S., Horányi, A., Muñoz-Sabater, J., Nicolas, J., Peubey, C., Radu, R., and Schepers, D.: The ERA5 global reanalysis, Quarterly Journal of the Royal Meteorological Society, 146, 1999-2049, 2020.

Hu, C., Griffis, T. J., Xia, L., Xiao, W., Liu, C., Xiao, Q., Huang, X., Yang, Y., Zhang, L., and Hou, B.: Anthropogenic CO2 emission reduction during the COVID-19 pandemic in Nanchang City, China, Environmental Pollution, 309, 119767, 2022.

Hu, Y. and Shi, Y.: Estimating CO2 emissions from large scale coal-fired power plants using OCO-2 observations and emission inventories, Atmosphere, 12, 811, 2021.

Kiemle, C., Ehret, G., Amediek, A., Fix, A., Quatrevalet, M., and Wirth, M.: Potential of spaceborne lidar measurements of carbon dioxide and methane emissions from strong point sources, Remote Sensing, 9, 1137, 2017.

Krings, T., Gerilowski, K., Buchwitz, M., Reuter, M., Tretner, A., Erzinger, J., Heinze, D., Pflüger, U., Burrows, J., and Bovensmann, H.: MAMAP–a new spectrometer system for column-averaged methane and carbon dioxide observations from aircraft: retrieval algorithm and first inversions for point source emission rates, Atmospheric Measurement Techniques, 4, 1735-1758, 2011.

Krings, T., Neininger, B., Gerilowski, K., Krautwurst, S., Buchwitz, M., Burrows, J. P., Lindemann, C., Ruhtz, T., Schüttemeyer, D., and Bovensmann, H.: Airborne remote sensing and in situ measurements of atmospheric CO_2 to quantify point source emissions, Atmospheric Measurement Techniques, 11, 721-739, 2018.

Lauvaux, T., Miles, N. L., Deng, A., Richardson, S. J., Cambaliza, M. O., Davis, K. J., Gaudet, B., Gurney, K. R., Huang, J., and O'Keefe, D.: High-resolution atmospheric inversion of urban CO2 emissions during the dormant season of the Indianapolis Flux Experiment (INFLUX), Journal of Geophysical Research: Atmospheres, 121, 5213-5236, 2016.

545 Letu, H., Nakajima, T. Y., and Nishio, F.: Regional-scale estimation of electric power and power plant CO2 emissions using defense meteorological satellite program operational linescan system nighttime satellite data, Environmental Science & Technology Letters, 1, 259-265, 2014.

Li, W., Zhang, S., and Lu, C.: Exploration of China's net CO2 emissions evolutionary pathways by 2060 in the context of carbon neutrality, Science of The Total Environment, 831, 154909, 2022.

550 Luther, A., Kleinschek, R., Scheidweiler, L., Defratyka, S., Stanisavljevic, M., Forstmaier, A., Dandocsi, A., Wolff, S., Dubravica, D., and Wildmann, N.: Quantifying CH 4 emissions from hard coal mines using mobile sun-viewing Fourier transform spectrometry, Atmospheric Measurement Techniques, 12, 5217-5230, 2019.

Menzies, R. T., Spiers, G. D., and Jacob, J.: Airborne laser absorption spectrometer measurements of atmospheric CO 2 column mole fractions: Source and sink detection and environmental impacts on retrievals, Journal of Atmospheric and oceanic 555 technology, 31, 404-421, 2014.

Miller, C., Crisp, D., DeCola, P., Olsen, S., Randerson, J., Michalak, A., Alkhaled, A., Rayner, P., Jacob, D. J., and Suntharalingam, P.: Precision requirements for space-based data, Journal of Geophysical Research: Atmospheres, 112, 2007.

Nassar, R., Hill, T. G., McLinden, C. A., Wunch, D., Jones, D. B., and Crisp, D.: Quantifying CO2 emissions from individual power plants from space, Geophysical Research Letters, 44, 10,045-010,053, 2017.

560 Nassar, R., Mastrogiacomo, J.-P., Bateman-Hemphill, W., McCracken, C., MacDonald, C. G., Hill, T., O'Dell, C. W., Kiel, M., and Crisp, D.: Advances in quantifying power plant CO2 emissions with OCO-2, Remote Sensing of Environment, 264, 112579, 2021.

Ohyama, H., Shiomi, K., Kikuchi, N., Morino, I., and Matsunaga, T.: Quantifying CO2 emissions from a thermal power plant based on CO2 column measurements by portable Fourier transform spectrometers, Remote Sensing of Environment, 267, 565 112714, 2021.

Panofsky, H. A. and Dutton, J. A.: Atmospheric turbulence. Models and methods for engineering applications, New York: Wiley, 1984.

Pasquill, F.: The estimation of the dispersion of windborne material. Meteor. Mag., 90, 33-49., 1976: Atmospheric dispersion parameters in Gaussian plume modeling, Part 11. Possible requirements for change in the Turner workbook values. EPA 570 Publication No, EPA-600/4-76-030b, Environmental Protection Agency, Research Triangle Park …, 1961.

Pasquill, F. and Smith, F. B.: Atmospheric diffusion, Ellis Horwood Chichester1983.

Peters, G. P., Marland, G., Le Quéré, C., Boden, T., Canadell, J. G., and Raupach, M. R.: Rapid growth in CO2 emissions after the 2008–2009 global financial crisis, Nature climate change, 2, 2-4, 2012.

Pillai, D., Gerbig, C., Kretschmer, R., Beck, V., Karstens, U., Neininger, B., and Heimann, M.: Comparing Lagrangian and 575 Eulerian models for CO 2 transport–a step towards Bayesian inverse modeling using WRF/STILT-VPRM, Atmospheric Chemistry and Physics, 12, 8979-8991, 2012.

Protocol, K.: United Nations framework convention on climate change, Kyoto Protocol, Kyoto, 19, 1-21, 1997.

Reuter, M., Buchwitz, M., Schneising, O., Krautwurst, S., O'Dell, C. W., Richter, A., Bovensmann, H., and Burrows, J. P.: Towards monitoring localized CO_2 emissions from space: co-located regional CO_2 and NO_2 enhancements observed by the
580 OCO-2 and S5P satellites, Atmospheric Chemistry and Physics, 19, 9371-9383, 2019.

Savić, S., Selakov, A., and Milošević, D.: Cold and warm air temperature spells during the winter and summer seasons and their impact on energy consumption in urban areas, Natural hazards, 73, 373-387, 2014.

Schwandner, F. M., Gunson, M. R., Miller, C. E., Carn, S. A., Eldering, A., Krings, T., Verhulst, K. R., Schimel, D. S., Nguyen, H. M., and Crisp, D.: Spaceborne detection of localized carbon dioxide sources, Science, 358, eaam5782, 2017.

585 Searchinger, T. D., Wirsenius, S., Beringer, T., and Dumas, P.: Assessing the efficiency of changes in land use for mitigating climate change, Nature, 564, 249-253, 2018.

Sheng, M., Lei, L., Zeng, Z.-C., Rao, W., Song, H., and Wu, C.: Global land 1° mapping dataset of XCO2 from satellite observations of GOSAT and OCO-2 from 2009 to 2020, Big Earth Data, 7, 170-190, 2023.

Shi, T., Han, G., Ma, X., Pei, Z., Chen, W., Liu, J., Zhang, X., Li, S., and Gong, W.: Quantifying strong point sources emissions
590 of CO2 using spaceborne LiDAR: Method development and potential analysis, Energy Conversion and Management, 292, 117346, 2023.

Taylor, T., O'Dell, C., Crisp, D., Kuze, A., Lindqvist, H., Wennberg, P., Chatterjee, A., Gunson, M., Eldering, A., and Fisher, B.: An 11-year record of XCO2 estimates derived from GOSAT measurements using the NASA ACOS version 9 retrieval algorithm, Earth Syst. Sci. Data, 14, 325-360, 2022.

595 Toja-Silva, F., Chen, J., Hachinger, S., and Hase, F.: CFD simulation of CO2 dispersion from urban thermal power plant: Analysis of turbulent Schmidt number and comparison with Gaussian plume model and measurements, Journal of Wind Engineering and Industrial Aerodynamics, 169, 177-193, 2017.

Tubiello, F. N., Salvatore, M., Ferrara, A. F., House, J., Federici, S., Rossi, S., Biancalani, R., Condor Golec, R. D., Jacobs, H., and Flammini, A.: The contribution of agriculture, forestry and other land use activities to global warming, 1990–2012,
600 Global change biology, 21, 2655-2660, 2015.

Turnbull, J. C., Karion, A., Davis, K. J., Lauvaux, T., Miles, N. L., Richardson, S. J., Sweeney, C., McKain, K., Lehman, S. J., and Gurney, K. R.: Synthesis of urban CO2 emission estimates from multiple methods from the Indianapolis Flux Project (INFLUX), Environmental science & technology, 53, 287-295, 2018.

Turner, A. J., Kim, J., Fitzmaurice, H., Newman, C., Worthington, K., Chan, K., Wooldridge, P. J., Köehler, P., Frankenberg,
605 C., and Cohen, R. C.: Observed impacts of COVID-19 on urban CO 2 emissions, Geophysical Research Letters, 47, e2020GL090037, 2020.

Waite, M., Cohen, E., Torbey, H., Piccirilli, M., Tian, Y., and Modi, V.: Global trends in urban electricity demands for cooling and heating, Energy, 127, 786-802, 2017.

Wolff, S., Ehret, G., Kiemle, C., Amediek, A., Quatrevalet, M., Wirth, M., and Fix, A.: Determination of the emission rates of
610 CO 2 point sources with airborne lidar, Atmospheric Measurement Techniques Discussions, 2020, 1-28, 2020.

Wu, D., Lin, J. C., Fasoli, B., Oda, T., Ye, X., Lauvaux, T., Yang, E. G., and Kort, E. A.: A Lagrangian approach towards extracting signals of urban CO 2 emissions from satellite observations of atmospheric column CO 2 (XCO 2): X-Stochastic Time-Inverted Lagrangian Transport model ("X-STILT v1"), Geoscientific Model Development, 11, 4843-4871, 2018.

Ye, X., Lauvaux, T., Kort, E. A., Oda, T., Feng, S., Lin, J. C., Yang, E. G., and Wu, D.: Constraining fossil fuel CO2 emissions from urban area using OCO‐2 observations of total column CO2, Journal of Geophysical Research: Atmospheres, 125, e2019JD030528, 2020.

Zhang, H., Han, G., Ma, X., Chen, W., Zhang, X., Liu, J., and Gong, W.: Robust algorithm for precise X CO2 retrieval using single observation of IPDA LIDAR, Optics Express, 31, 11846-11863, 2023.

Zhang, H., Han, G., Chen, W., Pei, Z., Liu, B., Liu, J., Zhang, T., Li, S., and Gong, W.: Validation Method for Spaceborne IPDA LIDAR X co 2 Products via TCCON, IEEE Journal of Selected Topics in Applied Earth Observations and Remote Sensing, 2024.

Zhang, T., Zhang, W., Yang, R., Liu, Y., and Jafari, M.: CO2 capture and storage monitoring based on remote sensing techniques: A review, Journal of Cleaner Production, 281, 124409, 2021.

Zheng, B., Chevallier, F., Ciais, P., Broquet, G., Wang, Y., Lian, J., and Zhao, Y.: Observing carbon dioxide emissions over China's cities and industrial areas with the Orbiting Carbon Observatory-2, Atmospheric Chemistry and Physics, 20, 8501-8510, 2020.

Zhu, Y., Yang, J., Zhang, X., Liu, J., Zhu, X., Zang, H., Xia, T., Fan, C., Chen, X., and Sun, Y.: Performance improvement of spaceborne carbon dioxide detection IPDA LIDAR using linearty optimized amplifier of photo-detector, Remote Sensing, 13, 2007, 2021.